RSC Advances

PAPER

View Article Online
View Journal | View Issue



Cite this: *RSC Adv.*, 2017, **7**, 43125

# Size-tunable $NaGdF_4$ nanoparticles as $T_2$ contrast agents for high-field magnetic resonance imaging†

Zhigao Lu,[ab] Ruijun Deng,[ab] Mingming Zhen,*[ab] Xue Li,[ab] Toujun Zou,[a] Yue Zhou,[ab] Mirong Guan,[a] Ying Zhang,[ab] Yuqing Wang,[c] Tong Yu,[ab] Chunying Shu[ab] and Chunru Wang *[ab]

Received 27th July 2017
Accepted 24th August 2017

DOI: 10.1039/c7ra08303c

rsc.li/rsc-advances

It is important to get high-quality magnetic resonance images at high magnetic field (>3 T) for medical diagnoses. However, the efficiency of the commonly used magnetic resonance imaging (MRI) contrast agents (CAs) always decrease with the increasing of magnetic field intensity. Thus, it is necessary to design MRI CAs with high relaxivity at high magnetic field. In this study, the hydrophilic and biocompatible $NaGdF_4$@$SiO_2$ nanoparticles (NPs) were feasibly synthesized and exhibited highly effective $T_2$ contrast imaging at 7 T magnetic field. Furthermore, the obtained NPs had a higher $r_2/r_1$ value than the other typical $T_2$ CAs (such as Dy-based NPs and Fe-based NPs) at high magnetic field. The observed large $r_2$ of the current $NaGdF_4$@$SiO_2$ was mainly ascribed to the increased particle sizes. For *in vivo* application, 250 nm $NaGdF_4$@$SiO_2$ (with the highest relaxivity) as $T_2$-weighted MRI CAs was further assessed. Toxicity studies demonstrated that $NaGdF_4$@$SiO_2$ NPs exhibited little toxicity both *in vitro* and *in vivo*. Therefore, $NaGdF_4$@$SiO_2$ NPs with appropriate size could be used as high-performance $T_2$ CAs in the high magnetic field.



## Introduction

Magnetic resonance imaging (MRI) has become one of the most powerful medical diagnostic tools in clinical bioimaging,[1,2] due to its non-invasive and non-radiative nature. It can realize the excellent visualization of anatomical details with superb spatial and temporal resolution. To improve the accuracy and specificity of the imaging pathological processes, the MRI CAs are often required in order to better distinguish malignant tumor tissues from normal tissues to diagnosis cancer or other pathological processes.[3–5] These CAs selectively shorten the $T_1$ or $T_2$ relaxation time in the region of interest, providing brighter or darker enhancement of the pathology. The efficiency of CAs relies on their $r_1$ ($1/T_1$) and $r_2$ ($1/T_2$) relaxivity values as well as the $r_2/r_1$ ratio.[6–8] The higher ratio of $r_2/r_1$, the better $T_2$ contrast efficiency.[6] Furthermore, in some preclinical MRI studies, such as blood vessels or small animal models, must provide the highest possible resolution; hence, they rely heavily on the high field strengths (>3.0 T).[9]

Lanthanide-based nanoparticles can be used as ideal building blocks for CAs because of their unique magnetic properties.[10–14] Among the lanthanide elements, paramagnetic gadolinium (Gd), which has seven unpaired electrons, is usually considered as excellent $T_1$-weighted MRI CAs.[15] Recently, gadolinium ion-doped nanoparticles (Gd-NPs), such as upconversion nanoparticles (UCNPs),[16–19] $GdPO_4$,[20,21] $GdF_3$ (ref. 22 and 23) and $Gd_2O_3$,[24,25] have attracted increasing attention as promising $T_1$ MRI CAs, more and more studies have been performed to describe how Gd-NPs affect the longitudinal relaxation rate ($r_1$) and have demonstrated that the surface-coating and the size of the Gd-NPs are key factors influencing the relaxation rate.[26–28] Unfortunately, many previously reported Gd-NPs including Dy-NPs and Fe-NPs have high $r_1$ or $r_2$ values but the $r_2/r_1$ value is not so satisfied. Furthermore, one of the major limitation of the present CAs is their decreased efficiency at higher magnetic fields, for example, the $T_1$ imaging ability of Gd ion complexes is optimal at fields below 1 T.[6,29,30] The other kind of $T_2$ CAs (superparamagnetic iron oxide nanoparticles) are known to saturate their magnetization at about 1.5 T. Therefore, the development of CAs (with high $r_2$ and high ratio of $r_2/r_1$) that are more efficient at high magnetic field is urgently needed to take full advantage of contrast enhanced MRI at ultrahigh fields and to meet the ever-growing performance demand on scientific research and clinical diagnosis.[31]

In this work, we report a simple and feasible approach to prepare the $NaGdF_4$ NPs by direct nanoprecipitation method for high efficiency $T_2$ MRI CAs. This synthesized method allows for

[a]*Beijing National Laboratory for Molecular Sciences, Laboratory of Molecular Nanostructure and Nanotechnology, CAS Research/Education Center for Excellence in Molecular Sciences, Institute of Chemistry, Chinese Academy of Sciences, Beijing 100190, China. E-mail: crwang@iccas.ac.cn*

[b]*University of Chinese Academy of Sciences, Beijing 100049, China*

[c]*CAS Key Laboratory for Biomedical Effects of Nanomaterials and Nanosafety, National Center for Nanoscience and Technology of China, Beijing, 100190, China*

† Electronic supplementary information (ESI) available. See DOI: 10.1039/c7ra08303c

regulating crystal growth by changing the density of chelator to obtain different sizes of $NaGdF_4$ NPs in the range of 100–220 nm. Then $NaGdF_4$ NPs with different size distribution were coated with the same thickness of silica (~12 nm), forming a highly biocompatible and hydrophilic rigid sphere with the diameter from 120 to 250 nm. The $T_2$ relaxivity measurements were performed at 0.5 T and 7 T. The $r_2$ values were 129–159 $mM^{-1}$ $s^{-1}$, and the $r_2/r_1$ values were as high as 173–586 (7 T) when the size of the NPs was increased. The magnetization plots (M–H) of the $NaGdF_4$@$SiO_2$ show that NPs are paramagnetic and the observed large $r_2$ of the current $NaGdF_4$@$SiO_2$ was mainly ascribed to the particle sizes increase. The toxicities of these NPs *in vitro* and *in vivo* were further evaluated using WST-8 assays and pathology staining methods to demonstrate the non-toxicity with the $NaGdF_4$@$SiO_2$ NPs. The $T_2$-weighted MRI contrast effect *in vivo* was also investigated. In short, this work will provide a new method for the application of Gd-NPs as high efficiency $T_2$ MRI CAs.

# Experiments

## Materials

All of the chemicals used were of analytical grade and were used without further purification unless otherwise stated. Gadolinium oxide ($Gd_2O_3$, 99.9%) was purchased from China Minmetals Corporation Co. Ltd. $Na_3$-nitrilotriacetic acid (Na-NTA, 99.9%) and sodium fluoride (NaF) were obtained from Aldrich. Tetraethyl orthosilicate (TEOS) was purchased from Alfa-Aesar. Aqueous ammonia solution (25 wt%), perchloric acid ($HClO_4$), and ethanol were purchased from Beijing Chemical Factory (China). Dulbecco's modified Eagle's medium (DMEM, HyClone, United States), Cell Counting Kit-8 (CCK-8), penicillin/streptomycin (PS), and fetal bovine serum (FBS, HyClone, USA) were all purchased from Biodee Co. Ltd., Beijing (China). This study was performed in strict accordance with the NIH guidelines for the care and use of laboratory animals (NIH publication no. 85-23 Rev. 1985) and was approved by IACUC (Institutional Animal Care and Use Committee) of Capital Medical University (Beijing, China).

## Preparation of $NaGdF_4$ nanoparticles

$NaGdF_4$ NPs were synthesized as follows. In brief, Gadolinium oxide (1 mmol) and a measured amount of perchloride were mixed together in a 50 mL flask heated to 80 °C until a clear solution formed. The gadolinium perchloride solution was cooled to room temperature and concentrated to 5 mL (0.2 mol $L^{-1}$) by vacuum rotary evaporation. Next, 15 mL of different concentrations of trisodium citrate (0.6 mol $L^{-1}$ for 120 nm NPs, 0.3 mol $L^{-1}$ for 190 nm NPs and 0.2 mol $L^{-1}$ for 250 nm NPs) was quickly injected into the flask, the mixture was stirred for 10 min. Then, NaF (5 mL, 0.5 mol $L^{-1}$) was quickly injected into the flask with vigorous magnetic stirring at room temperature for 4 h and a milk white solution formed. Subsequently, the milk white solution was centrifuged at 8000 rpm and washed twice with ethanol and water. The NPs were finally dispersed in 15 mL of water.

## Preparation of silica-coated $NaGdF_4$ nanoparticles

$NaGdF_4$@$SiO_2$ core/shell nanoparticles were prepared by the reverse microemulsion method.[15,32] The preparation was typically performed as follows: under vigorous stirring, 1 mL of aqueous $NaGdF_4$ solution was introduced into a liquid system containing 10 mL of ethanol, the volume of aqueous ammonia solutions and TEOS were added differently along with different size of $NaGdF_4$@$SiO_2$ NPs: for 120 nm $NaGdF_4$@$SiO_2$ NPs, 40 μL aqueous ammonia solutions were added dropwise, after about 5 minutes, another 50 μL TEOS were introduced dropwise into the flask, for 190 nm and 250 nm $NaGdF_4$@$SiO_2$ NPs, the procedures were the same as 120 nm $NaGdF_4$@$SiO_2$ NPs, but the volume were that: 60 μL aqueous ammonia solutions and 80 μL TEOS for 190 nm $NaGdF_4$@$SiO_2$ NPs, 80 μL aqueous ammonia solutions and 100 μL TEOS for 250 nm $NaGdF_4$@$SiO_2$ NPs. Then, the reaction system was sealed and kept under stirring in a dark at room temperature for different times (4 h, $d = 120$ nm; 5 h, $d = 190$ nm; 6 h, $d = 250$ nm). Isopropanol was used to terminate the reaction, and the resultant precipitate of $NaGdF_4$@$SiO_2$ composite particles was subsequently washed in sequence with ethanol and water. The particles suspended in liquid media were typically collected by centrifugation and then dispersed in pure water for further characterization.

## Characterization

Transmission electron microscopy (TEM) images were obtained on a JEM-2100F microscope (JEOL, Japan) at an operating voltage of 100 kV. Samples were prepared by spreading a drop of sample on copper grids, followed by evaporation under vacuum. Powder X-ray diffraction (XRD) measurements were taken with a Rigaku D/MAX-2000 diffractometer (Japan) with a slit of 1/2° at a scanning rate of 2° $min^{-1}$ using Cu Kα radiation ($\lambda = 0.15406$ nm). The dynamic light scattering (DLS, Malvern, UK) measurements were performed at 25 °C. The scattering angle was fixed at 90°. Samples were filtered through a 0.45 μm pore size membrane before DLS measurement.

## Cell culture

Human lung cancer A549 cells were provided by peking union medical college hospital (Beijing, China). A549 cells were cultured in DMEM supplemented with 10% fetal bovine serum (FBS), streptomycin (100 μg $mL^{-1}$) and penicillin (100 U $mL^{-1}$) at 37 °C in a humidified 5% $CO_2$ atmosphere.

## Cellular toxicity

To investigate the cellular toxicity of $NaGdF_4$@$SiO_2$, the A549 cells were seeded in a 96-well culture plate with DMEM for 24 h. Then, the aged culture medium was replaced with freshly prepared culture medium that contained $NaGdF_4$@$SiO_2$ solution in a series of gradient $Gd^{3+}$ concentrations and incubated for another 24 h ($n = 6$). Subsequently, the culture medium was removed, and 100 μL of DMEM without phenol red and 10 μL of Cell Counting Kit-8 (CCK-8; DOJINDO, Kumamoto, Japan) were added to each well. After incubation for another 1 h, the

 

absorbance of each treated well was measured at 450 nm using a microplate reader (iMarkmicroplate reader, Bio-RAD, USA).

### Relaxivity measurement *in vitro*

To evaluate the contrast enhancement of the obtained $NaGdF_4$@$SiO_2$, the relaxivities $r_1$ and $r_2$ were measured at 0.5 T and 7 T. For 0.5 T NM120 analyst, using a spin-echo pulse sequence with pulse repetition time $D_0$ = 300 ms. For 7 T analyst, the MR signal intensity in the tubes was ascertained by the average intensity in the defined regions of interests (ROI) using a 7 T (BioSpec70/20USR, Bruker, Germany) in conjunction with a volume coil. Dilutions of $NaGdF_4$@$SiO_2$ in water were placed in a series of 0.5 mL tubes. The $T_1$ WI and $T_2$ WI were acquired with $T_1$-flash and $T_2$-turbo-RARE sequences, respectively. The $T_1$-flash parameters were as follows: TR/TE = 150/1.8 ms, NEX = 3, flap angle = 80°, FOV = 40 × 40 mm, MTX = 256 × 256; $T_2$-turbo-RARE: TR/TE = 2500/53.38 ms, NEX = 1, flap angle = 90°, FOV = 40 × 40 mm, MTX = 256 × 256. The $T_1$ and $T_2$ values were measured with $T_1$ map-RARE and $T_2$ map-MSME sequences, respectively. The $T_1$ map-RARE parameters were as follows: TR/TE = 189, 400, 800, 1200, 2500/6.1 ms, NEX = 1, flap angle = 90°, FOV = 40 × 40 mm, MTX = 128 × 128; $T_2$ map-MSME: TR/TE = 2500/6.67 (16 echo times, the step is 6.67 ms), NEX = 1, flap angle = 90°, FOV = 40 × 40 mm, MTX = 128 × 128.

### Magnetic resonance imaging *in vivo*

H22 cells were grown in DMEM medium that was supplemented with 10% FBS and 1% PS at 37 °C in 5% $CO_2$. Balb/c mice (five weeks, 18–22 g) were purchased from Beijing Xing Long Biological Technology Co., Ltd (China). Each mouse was subcutaneously injected in the flank with approximately $8 \times 10^6$ H22 cells that were suspended in 100 μL of PBS. Approximately 8 d after inoculation, 200 μL of the complex solution at a dose of 4 mM $Gd^{3+}$ was intravenously injected *via* the tail vein and mice were imaged with a rat head coil on a 7 T MRI instrument. The $T_2$ WI was acquired with $T_2$-turbo-RARE sequence. The parameters were as follows: TR/TE = 3000/50 ms, NEX = 2, flap angle = 90°, FOV = 40 × 40 mm, MTX = 256 × 256.

### H&E stainning

For hematoxylin and eosin (H&E) staining, the heart, liver, spleen, lung, and kidney were harvested from mice after intravenously injected with different sizes of $NaGdF_4$@$SiO_2$ NPs ($n$ = 3, dose = 4 mM, 200 μL, test group) and the un-treated mice as control. The tissues were fixed in 4% paraformaldehyde solution and embedded in paraffin. They were then sectioned and stained with hematoxylin and eosin. The histological sections were tested for *in vivo* toxicity and observed under a NanoZoomer-SQ slide scanner (Hamamatsu, Japan).

## Results and discussion

### Synthesis and characterization of $NaGdF_4$ NPs

$NaGdF_4$ NPs were first formed by the aggregation model and were prepared in the presence of a chelator (trisodium citrate).

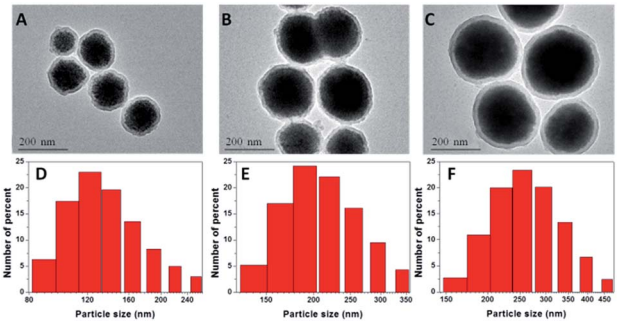


Fig. 1 TEM images of silica-coated $NaGdF_4$ NPs, sample 1 (A), sample 2 (B), and sample 3 (C); particle size distributions for sample 1 (D): 120 ± 25 nm; sample 2 (E): 190 ± 30 nm; and sample 3 (F): 250 ± 50 nm as measured by DLS.

By changing the concentration of trisodium citrate from 0.2 M to 0.6 M, the sizes of obtained $NaGdF_4$ NPs were ranged from 100 nm to 220 nm (Fig. S1†). According to the reported literature,[33] the formation of the NPs is primarily controlled by the aggregation of the primary Gd ion. Smaller particles were achieved by the presence of the chelator trisodium citrate and its variation ion concentration. This change probably resulted in the adsorption of chelators onto the $NaGdF_4$ nanoparticles and influenced the repulsive force between the primary Gd ions, preventing the primary Gd ions from forming large particles but generating uniform NPs by aggregation. The water-dispersible $NaGdF_4$ NPs were then coated with silicon dioxide, as shown in Fig. 1A–C. The silica-coated $NaGdF_4$ NPs were well dispersed in water. By changing the ratio of TEOS to ammonia, different sizes of $NaGdF_4$ were coated with the same thickness of silica, and the thickness of the silica layer could be easily observed by TEM as approximately 12 nm. The average hydrodynamic diameters of the $NaGdF_4$@$SiO_2$ NPs were ranged from 120 nm to 250 nm measured by dynamic light scattering (DLS, Fig. 1D–F), which was consistent with those observed with TEM. The surface zeta potential of $NaGdF_4$@$SiO_2$ with the size of 250 nm was −30 ± 0.6 mV, −32 ± 0.8 mV for 190 nm NPs and

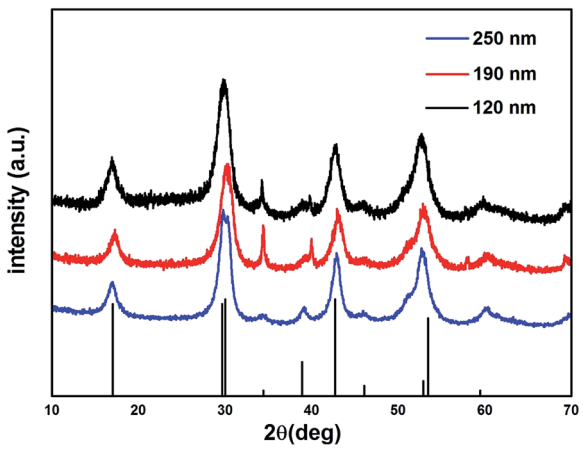


Fig. 2 XRD patterns of $NaGdF_4$ sample 1 (120 nm), sample 2 (190 nm), sample 3 (250 nm) and JCPDS #27-0699.

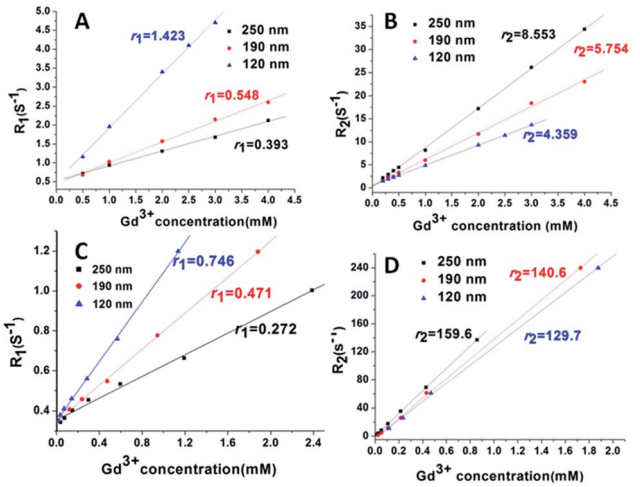


Fig. 3 Relaxation rate $r_1$ ($1/T_1$) *versus* $Gd^{3+}$ concentration at different magnetic field strengths, 0.5 T (A) and 7 T (C). Relaxation rate $r_2$ ($1/T_2$) *versus* $Gd^{3+}$ concentration at different magnetic field strengths, 0.5 T (B) and 7 T (D). Blue triangle stands for sample 1; red circle stands for sample 2 and black square stands for sample 3.

−35 ± 1.1 mV for 120 nm NPs. Thus, three kinds of $NaGdF_4$@$SiO_2$ NPs with different size distribution were prepared and shortened as sample 1 ($NaGdF_4$@$SiO_2$ 120 nm), sample 2 ($NaGdF_4$@$SiO_2$ 190 nm) and sample 3 ($NaGdF_4$@$SiO_2$ 250 nm).

The crystalline information on $NaGdF_4$ NPs was provided by powder X-ray diffraction (XRD, Fig. 2). The peak position and relative intensity of all the $NaGdF_4$ NPs were in good agreement with the data of hexagonal-phase $NaGdF_4$ crystals (β-$NaGdF_4$) as reported in the JCPDS standard card (27-0699), and no impurity phase was detected.

### Relaxivity measurements and $T_2$-weighted MRI *in vitro*

To evaluate the impact of size on MRI relaxivity properties, the $r_1$ and $r_2$ relaxivity of $NaGdF_4$@$SiO_2$ NPs were investigated in water at 0.5 T and 7 T. To calculate the ionic relaxivities, the Gd ion concentration of the $NaGdF_4$@$SiO_2$ NPs dispersions was determined using ICP-MS after digesting the NPs with concentrated nitric acid and hydrochloric acid (v/v = 1 : 3) at 100 °C overnight. The ionic relaxivity values ($r_1$, $r_2$) with an equivalent Gd ion concentration range of 0–2.5 mM at 0.5 T and 7 T were obtained from the slope of the linear regression fit from the relaxivity plots (Fig. 3). In addition, $r_1$ and $r_2$ relaxivity values of $NaGdF_4$@$SiO_2$ were shown in Table S1.† At 0.5 T, $r_1$ relaxivities decreased with the increase of particle size, from a value of 1.4 $mM^{-1}$ $s^{-1}$ (120 nm particles) to 0.39 $mM^{-1}$ $s^{-1}$ (250 nm particles). At 7 T, $r_1$ relaxivities decreased from a value of 0.75 $mM^{-1}$ $s^{-1}$ (for the 120 nm particles) to 0.27 $mM^{-1}$ $s^{-1}$ (for the 250 nm particles). Conversely, at both 0.5 T and 7 T, $r_2$ relaxivities increased dramatically with increasing particle size, from a value of 4.36 $mM^{-1}$ $s^{-1}$ for the 120 nm particles to 8.55 $mM^{-1}$ $s^{-1}$ for the 250 nm particles at 0.5 T, and from a value of 129.7 $mM^{-1}$ $s^{-1}$ for the 120 nm particles to 159.6 $mM^{-1}$ $s^{-1}$ for the 250 nm particles at 7 T. Clearly, the $r_2$ values were highly increased at high field strengths. The $r_2$ value is as high as some reported $Dy^{3+}$-based NPs and some of clinically used $T_2$ CAs[6,34–40] (Table 1).

According to the $r_2$ relaxivities measured at both 0.5 T and 7 T, larger size of $NaGdF_4$@$SiO_2$ show higher relaxivity than the smaller ones. The magnetic hysteresis loop plot (M–H) obtained by different size of NPs showed that NPs are paramagnetic and the observed high $r_2$ of the current $NaGdF_4$@$SiO_2$ mainly be ascribed to the particle sizes increase (Fig. S2†). To further analyze the observed enhancement of ionic relaxivity with increasing NP size, the relaxivities, based on the mass concentration of NPs ($r_1$/M) and CAs concentration of NPs ($r_1$/NP), were calculated from the ionic relaxivity ($r_1$/[$Gd^{3+}$]) (Table S2†).[26]

The $r_2$/NP values correspond to per CA relaxivity, and the relaxivity increases from $1.56 \times 10^9$ $mM^{-1}$ $s^{-1}$ for the 120 nm particle to $1.73 \times 10^{10}$ $mM^{-1}$ $s^{-1}$ for the 250 nm particles at 7 T. Because the total number of Gd ions is higher in larger particles, the $r_2$/NP values increase with size. Clinical complexes typically contain one Gd ion per CA, and their unit CA relaxivity is the same as their ionic relaxivity. Thus, the relaxivity offered by each $NaGdF_4$ NP described here is approximately $1 \times 10^9$ times that of clinical agents, which allows enhanced local contrast and was highly beneficial for targeted imaging. Moreover, because of the coating of silica on the $NaGdF_4$, bundles of multiple Gd ions in a crystalline NPs are less likely to leak. ICP-MS analysis of the bulk water after dialysis of the NPs showed no appreciable amount of free Gd ions in solution, indicating

Table 1 Comparison of $NaGdF_4$@$SiO_2$ NPs and the clinically used MRI $T_2$ CAs

| Contrast agents | Surface coating | Size (nm) | HD (nm) | $r_2$ ($mM^{-1}$ $s^{-1}$) | $r_1$ ($mM^{-1}$ $s^{-1}$) | $r_2/r_1$ | Field (T) | Ref. |
|---|---|---|---|---|---|---|---|---|
| $NaGdF_4$@$SiO_2$ | $SiO_2$ | 100 | 120 | 129.7 | 0.746 | 173.8 | 7 | This work |
| $NaGdF_4$@$SiO_2$ | $SiO_2$ | 160 | 190 | 142.9 | 0.471 | 303.4 | 7 | |
| $NaGdF_4$@$SiO_2$ | $SiO_2$ | 220 | 250 | 159.6 | 0.272 | 586.8 | 7 | |
| $NaDyF_4$ NP | PMAO–PEG | 20.3 | 33.7 | 101 | 0.33 | 306 | 9.4 | 6 |
| Dy-fullerenol [$Dy@C_{82}(OH)_n$] | | | | 20 | 0.95 | 21 | 9.4 | 40 |
| Dy-DTPA-PcHexPh$_2$ | | | | 3 | 0.11 | 27 | 7 | 39 |
| $Dy_2O_3$ | D-glu, acid | 3 | | 40.28 | 0.16 | 251 | 3 | 35 |
| Combidex ($Fe_3O_4$) | Dextran | 5.85 | 35 | 60 | 10 | 6 | 1.5 | 37 |
| Feridex ($Fe_3O_4$, γ-$Fe_2O_3$) | Dextran | 4.96 | 160 | 93 | 4.1 | 22 | 3 | 38 |
| Resovist ($Fe_3O_4$) | Carboxydextran | 4 | 60 | 143 | 4.6 | 31 | 3 | 38 |
| α-Fe | PEG | 10 | | 129 | 1.4 | 92 | 1.5 | 36 |

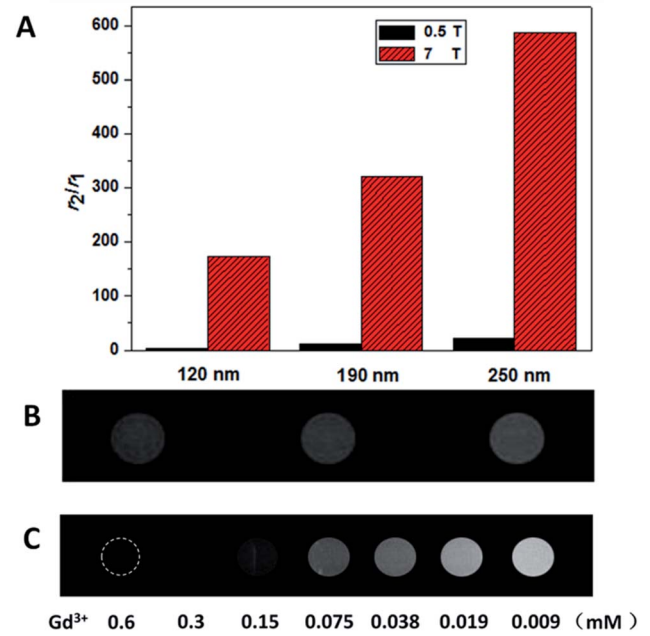


Fig. 4 (A) Comparison of $r_2/r_1$ values with different sizes at 0.5 T and 7 T. (B) Phantom images of the NPs with sizes ranging from 250 nm to 120 nm (left to right) at a concentration of 0.1 mM $Gd^{3+}$ at 7 T. (C) Concentration-dependent phantom image contrast of the 120 nm NPs at 7 T.

that no leaking of ions from the NP occurred. Thus, these NPs are good scaffolds for integrating multiple Gd ions without compromising Gd ion binding.

The ability of CAs to be used as $T_2$ agents was also governed by the ratio of their transverse relaxivity to longitudinal relaxivity, high $r_2/r_1$ ratios were considered ideal. The $r_2/r_1$ ratio for the 120 nm NPs was approximately 157, and the 250 nm NPs was as high as approximately 587 (Fig. 4A), which to the best of our knowledge, was the highest value reported for Gd-based nanoparticle CAs thus far.

For $T_2$-weighted MRI *in vitro*, the $T_2$-weighted phantom MR images between the three types of $NaGdF_4$@$SiO_2$ NPs were obtained at 7 T. As shown in Fig. 4B, the images of three types NPs (all at a 0.1 mM $Gd^{3+}$ concentration) became shallow as the size gets smaller (from left to right). The 250 nm $NaGdF_4$@$SiO_2$ NPs, which had shown the highest relaxivity and may suit for biological applications were chosen for concentration-dependent (0.6–0.009 mM $Gd^{3+}$) phantom images to examine the feasibility of the NPs for *in vitro* MR imaging.[41] As we can easily find that (Fig. 4C), with Gd ion concentrations decreased (from left to right), the $T_2$-weighted.

MRI images became shallow continuously. It is evident that these NPs have excellent $T_2$-weighted MR imaging ability and can easily be tuned by adjusting the size and concentration of the NPs.

### $T_2$-weighted MRI *in vivo*

Due to the excellent $T_2$ magnetic resonance effect of $NaGdF_4$@$SiO_2$ NPs, the applicability as a $T_2$-weighted MRI CAs *in vivo* was further assessed. Therefore, 250 nm $NaGdF_4$@$SiO_2$ NPs (with the highest $r_2$ relaxivities) were chosen for intravenous injection in tumor-bearing (H22) mouse model. Compared with the MR images of tumor and normal tissue before 7 h and 24 h post-injection, remarkable negative contrast enhancement was observed in the tumor region, whereas hardly any changes appeared in the normal tissue (Fig. 5). According to the MR images, NPs could accumulate in the tumor and decreased in 24 h. It demonstrated silica coated $NaGdF_4$ NPs have good biocompatibility and can be accumulated at the tumor position through the enhanced permeability and retention (EPR) effect.[41,42] These result indicated that $NaGdF_4$@$SiO_2$ NPs (250 nm) could act as high-performance $T_2$-weighted MRI CAs on H22 tumor *in vivo*. Furthermore, $NaGdF_4$@$SiO_2$ NPs (250 nm) in the main organs at different time points post-injection have been investigated. After they were intravenously injected with the NPs, the mice were sacrificed at 2 h, 7 h, 24 h, and 30 day post-injection. The distribution of $Gd^{3+}$ in each organ was shown in Fig. 6. The results exhibited that 250 nm $NaGdF_4$@$SiO_2$ NPs mainly accumulated in the lung, liver and spleen and reached a maximum at 7 h post-injection in the tumor, which was consistent with the above MRI results. After 30 day post-injection, the $Gd^{3+}$ residues were nearly undetectable in the organs *via* ICP-MS, showing that most of the NPs were excreted from the body of the mice.

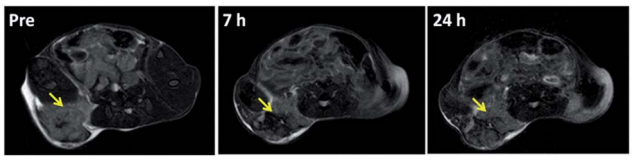


Fig. 5 *In vivo* $T_2$-weighted MR images of H22 tumor-bearing mice obtained before and 7 h, 24 h after tail intravenous injection of sample 3 (200 μL, 4 mM), yellow arrow point to the tumor area.

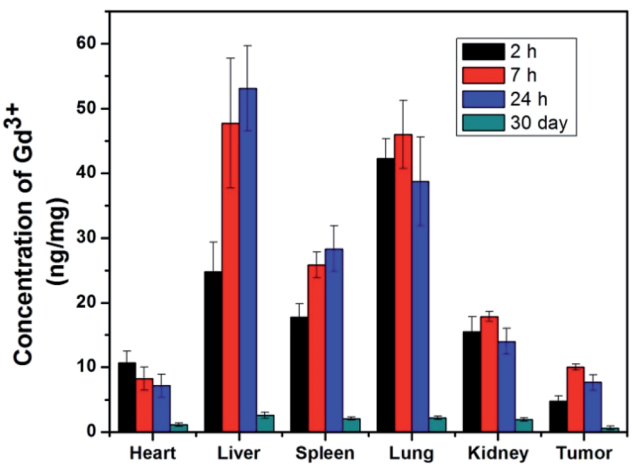


Fig. 6 The biodistribution of 250 nm $NaGdF_4$@$SiO_2$ NPs *in vivo*. $NaGdF_4$@$SiO_2$ (4 mM, 200 μL) was intravenously injected into the mouse ($n = 4$).

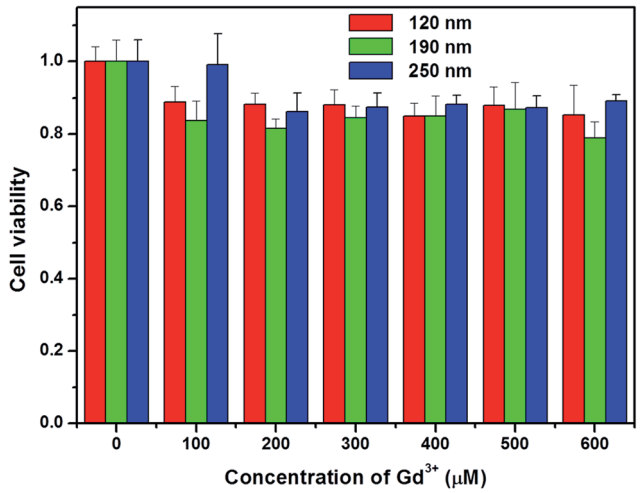


Fig. 7 Viability of A549 cells after treatment with different concentrations of $NaGdF_4$@$SiO_2$ NPs with different $Gd^{3+}$ concentrations (0, 100 μM, 200 μM, 300 μM, 400 μM, 500 μM and 600 μM) for 24 h. The viability was determined by CCK-8 assay. Error bar represents the standard error of 6 trials.

### Toxicity of $NaGdF_4$@$SiO_2$

To evaluate the toxicity of silica-coated $NaGdF_4$ NPs, the cell growth and viability of A549 cells incubated with $NaGdF_4$@$SiO_2$ at different $Gd^{3+}$ concentrations (up to 600 μM) for 24 h were evaluated. The WST-8 assay showed that no significant differences in the proliferation of A549 cells were observed in the absence or presence of $NaGdF_4$@$SiO_2$ within 24 h (Fig. 7). Even at the concentration of 600 μM, the cell viability was estimated to be approximately 80%. The WST-8 assay results demonstrated that $NaGdF_4$@$SiO_2$ NPs showed low cytotoxicity to A549 cells.

Toxicity was further investigated by pathology assessments of tissue obtained from the tested mice at 7 days post-injection. The major organs such as heart, liver, spleen, lung and kidney were harvested for histological analysis. Despite the high-concentration injection of water dispersible $NaGdF_4$@$SiO_2$ NPs at an equivalent $Gd^{3+}$ concentration of 4 mM, no noticeable signs of organ damage or inflammatory lesions were observed in these major organs compared with the control (Fig. 8). This phenomenon has previously been observed in other rare-earth fluoride hosts. However, further long-term study is still needed to evaluate the toxicity of $NaGdF_4$-based MRI probes.

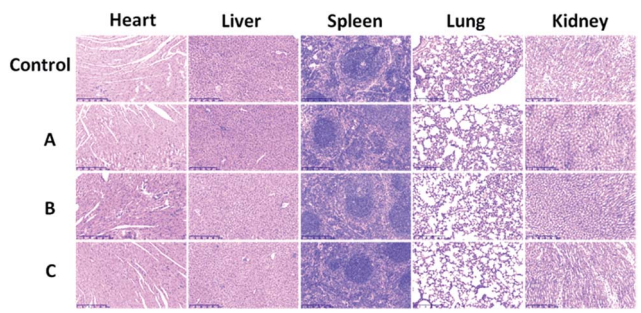


Fig. 8 H&E-stained tissue (heart, liver, spleen, lung, kidney. Scale bar: 250 μm) sections from mice intravenously injected with sample 1 (A), sample 2 (B), sample 3 (C) (200 μL, 0.9% NaCl, control) and (200 μL, dose = 4 mM $NaGdF_4$@$SiO_2$, test).

## Conclusion

In summary, we have prepared different sizes of $NaGdF_4$@$SiO_2$ NPs (from 120 nm to 250 nm), compared with Dy-based and Fe-based NPs, $NaGdF_4$@$SiO_2$ exhibited excellent high $r_2$ value and ultrahigh $r_2/r_1$ values at the high magnetic field (7 T). Furthermore, the results of toxicity studies indicated that $NaGdF_4$@$SiO_2$ NPs showed good compatibility and low cytotoxicity to the living systems. Our study demonstrated that Gd-based NPs with appropriate size could be used as potential $T_2$ CAs in an ultrahigh field.

## Conflicts of interest

There are no conflicts to declare.

## Acknowledgements

This work is supported by the National Natural Science Foundation of China (No. 51472248), the Key Research Program of the Chinese Academy of Sciences (QYZDJ-SSW-SLH025, KGZD-EW-T02, XDA09030302).

## References

1 H. B. Na, I. C. Song and T. Hyeon, *Adv. Mater.*, 2009, **21**, 2133–2148.
2 S. Viswanathan, Z. Kovacs, K. N. Green, S. J. Ratnakar and A. D. Sherry, *Chem. Rev.*, 2010, **110**, 2960–3018.
3 M. F. Dumont, C. Baligand, Y. Li, E. S. Knowles, M. W. Meisel, G. A. Walter and D. R. Talham, *Bioconjugate Chem.*, 2012, **23**, 951–957.
4 J. W. Bulte and D. L. Kraitchman, *NMR Biomed.*, 2004, **17**, 484–499.
5 J. Zeng, L. Jing, Y. Hou, M. Jiao, R. Qiao, Q. Jia, C. Liu, F. Fang, H. Lei and M. Gao, *Adv. Mater.*, 2014, **26**, 2694–2698.
6 G. K. Das, N. J. Johnson, J. Cramen, B. Blasiak, P. Latta, B. Tomanek and F. C. van Veggel, *J. Phys. Chem. Lett.*, 2012, **3**, 524–529.
7 E. Gultepe, F. J. Reynoso, A. Jhaveri, P. Kulkarni, D. Nagesha, C. Ferris, M. Harisinghani, R. B. Campbell and S. Sridhar, *Nanomedicine*, 2010, **5**, 1173–1182.
8 J. Qin, S. Laurent, Y. S. Jo, A. Roch, M. Mikhaylova, Z. M. Bhujwalla, R. N. Muller and M. Muhammed, *Adv. Mater.*, 2007, **19**, 1874–1878.
9 R. Weissleder, *Science*, 2006, **312**, 1168–1171.
10 J. Zhou, Y. Sun, X. Du, L. Xiong, H. Hu and F. Li, *Biomaterials*, 2010, **31**, 3287–3295.
11 J. Zhou, M. Yu, Y. Sun, X. Zhang, X. Zhu, Z. Wu, D. Wu and F. Li, *Biomaterials*, 2011, **32**, 1148–1156.
12 J. Zhou, X. Zhu, M. Chen, Y. Sun and F. Li, *Biomaterials*, 2012, **33**, 6201–6210.

13 M. He, P. Huang, C. Zhang, H. Hu, C. Bao, G. Gao, R. He and D. Cui, *Adv. Funct. Mater.*, 2011, **21**, 4470–4477.
14 J. Zhou, Z. Lu, G. Shan, S. Wang and Y. Liao, *Biomaterials*, 2014, **35**, 368–377.
15 F. Chen, W. Bu, S. Zhang, J. Liu, W. Fan, L. Zhou, W. Peng and J. Shi, *Adv. Funct. Mater.*, 2013, **23**, 298–307.
16 H. Du, J. Yu, D. Guo, W. Yang, J. Wang and B. Zhang, *Langmuir*, 2016, **32**, 1155–1165.
17 S. Biju, M. Harris, L. V. Elst, M. Wolberg, C. Kirschhock and T. N. Parac-Vogt, *RSC Adv.*, 2016, **6**, 61443–61448.
18 Z. Yi, X. Li, Z. Xue, X. Liang, W. Lu, H. Peng, H. Liu, S. Zeng and J. Hao, *Adv. Funct. Mater.*, 2015, **25**, 7119–7129.
19 M. Guan, H. Dong, J. Ge, D. Chen, L. Sun, S. Li, C. Wang, C. Yan, P. Wang and C. Shu, *NPG Asia Mater.*, 2015, **7**, e205.
20 Q. Du, Z. Huang, Z. Wu, X. Meng, G. Yin, F. Gao and L. Wang, *Dalton Trans.*, 2015, **44**, 3934–3940.
21 W. Ren, G. Tian, L. Zhou, W. Yin, L. Yan, S. Jin, Y. Zu, S. Li, Z. Gu and Y. Zhao, *Nanoscale*, 2012, **4**, 3754–3760.
22 X.-Y. Zheng, L.-D. Sun, T. Zheng, H. Dong, Y. Li, Y.-F. Wang and C.-H. Yan, *Sci. Bull.*, 2015, **60**, 1092–1100.
23 Y. Tian, H.-Y. Yang, K. Li and X. Jin, *J. Mater. Chem.*, 2012, **22**, 22510.
24 T. Shen, Y. Zhang, A. M. Kirillov, H. Cai, K. Huang, W. Liu and Y. Tang, *Chem. Commun.*, 2016, **52**, 1447–1450.
25 B. Babić-Stojić, V. Jokanović, D. Milivojević, M. Požek, Z. Jagličić, D. Makovec, K. Arsikin and V. Paunović, *J. Magn. Magn. Mater.*, 2016, **403**, 118–126.
26 N. J. J. Johnson, W. Oakden, G. J. Stanisz, R. Scott Prosser and F. C. J. M. van Veggel, *Chem. Mater.*, 2011, **23**, 3714–3722.
27 Y. Zhang, T. Zou, M. Guan, M. Zhen, D. Chen, X. Guan, H. Han, C. Wang and C. Shu, *ACS Appl. Mater. Interfaces*, 2016, **8**, 11246–11254.
28 M. Zhen, J. Zheng, L. Ye, S. Li, C. Jin, K. Li, D. Qiu, H. Han, C. Shu, Y. Yang and C. Wang, *ACS Appl. Mater. Interfaces*, 2012, **4**, 3724–3729.
29 P. Caravan, *Chem. Soc. Rev.*, 2006, **35**, 512–523.
30 L. Helm, *Future Med. Chem.*, 2010, **2**, 385–396.
31 E. Terreno, D. D. Castelli, A. Viale and S. Aime, *Chem. Rev.*, 2010, **110**, 3019–3042.
32 H. S. Qian, H. C. Guo, P. C. Ho, R. Mahendran and Y. Zhang, *Small*, 2009, **5**, 2285–2290.
33 Z. P. Chen, Y. Zhang, K. Xu, R. Z. Xu, J. W. Liu and N. Gu, *J. Nanosci. Nanotechnol.*, 2008, **8**, 6260–6265.
34 G. K. Das, Y. Zhang, L. D'Silva, P. Padmanabhan, B. C. Heng, J. S. Chye Loo, S. T. Selvan, K. K. Bhakoo and T. T. Yang Tan, *Chem. Mater.*, 2011, **23**, 2439–2446.
35 K. Kattel, J. Y. Park, W. Xu, H. G. Kim, E. J. Lee, B. A. Bony, W. C. Heo, J. J. Lee, S. Jin, J. S. Baeck, Y. Chang, T. J. Kim, J. E. Bae, K. S. Chae and G. H. Lee, *ACS Appl. Mater. Interfaces*, 2011, **3**, 3325–3334.
36 C. G. Hadjipanayis, M. J. Bonder, S. Balakrishnan, X. Wang, H. Mao and G. C. Hadjipanayis, *Small*, 2008, **4**, 1925–1929.
37 Y. X. Wang, *Quant. Imaging Med. Surg.*, 2011, **1**, 35–40.
38 M. Rohrer, H. Bauer, J. Mintorovitch, M. Requardt and H. J. Weinmann, *Invest. Radiol.*, 2005, **40**, 715–724.
39 P. Caravan, M. T. Greenfield and J. W. M. Bulte, *Magn. Reson. Med.*, 2001, **46**, 917–922.
40 H. Kato, Y. Kanazawa, M. Okumura, A. Taninaka, T. Yokawa and H. Shinohara, *J. Am. Chem. Soc.*, 2003, **125**, 4391–4397.
41 S. D. Perrault, C. Walkey, T. Jennings, H. C. Fischer and W. C. Chan, *Nano Lett.*, 2009, **9**, 1909–1915.
42 T. Stylianopoulos and R. K. Jain, *Nanomedicine*, 2015, **11**, 1893–1907.